Check for updates

OPEN

Arterial pulsations drive oscillatory flow of CSF but not directional pumping

Ravi Teja Kedarasetti[1,2], Patrick J. Drew[1,2,3,4] & Francesco Costanzo[1,2,3,5] ✉

The brain lacks a traditional lymphatic system for metabolite clearance. The existence of a "glymphatic system" where metabolites are removed from the brain's extracellular space by convective exchange between interstitial fluid (ISF) and cerebrospinal fluid (CSF) along the paravascular spaces (PVS) around cerebral blood vessels has been controversial. While recent work has shown clear evidence of directional flow of CSF in the PVS in anesthetized mice, the driving force for the observed fluid flow remains elusive. The heartbeat-driven peristaltic pulsation of arteries has been proposed as a probable driver of directed CSF flow. In this study, we use rigorous fluid dynamic simulations to provide a physical interpretation for peristaltic pumping of fluids. Our simulations match the experimental results and show that arterial pulsations only drive oscillatory motion of CSF in the PVS. The observed directional CSF flow can be explained by naturally occurring and/or experimenter-generated pressure differences.

The flow of cerebrospinal fluid (CSF) in the brain is hypothesized to play an important role in the clearance of metabolic waste and maintenance of the ionic environment[1–3]. Recent work suggests that the paravascular spaces (PVS) surrounding cerebral arteries provide a low-resistance pathway for the bulk flow of CSF into the brain[1,4–7]. However, this idea that there is bulk fluid movement into the brain is highly controversial, with both simulations[8–10] and experiments[6,7,11,12] being put forward both in support of and against bulk flow. One of the leading theories in support of bulk flow in the PVS identifies "peristaltic pumping" as the flow driver, *i.e.*, the idea that heartbeat-driven pulsations pump CSF in the PVS. Peristaltic pumping in a deformable tube is achieved by repeated contractions and dilations propagating along the wall of the tube. In fluid dynamics, peristaltic pumping is a well-understood mechanism of fluid transport. The mechanism of peristaltic pumping of fluids was first demonstrated by Latham[13]. Further work on the peristaltic pumping of fluids has encompassed a wide range of scenarios[14–17]. Calculations made using fluid dynamic principles can make very accurate predictions of fluid flow under peristalsis, and have been used in designing artificial peristaltic pumps[18–20].

Recent work by Mestre *et al.*[7] and Bedussi *et al.*[6] used *in vivo* two-photon microscopy[21] to simultaneously measure arterial pulsations and the flow of CSF in the PVS around the middle cerebral artery (MCA) by tracking the motion of fluorescent microspheres. They found that movement of CSF in the PVS had two components, a constant flow in the direction of blood flow with an average velocity of approximately 20 μm/sec, and an oscillatory flow in phase with the arterial pulsations[6,7], with a peak velocity of approximately 10 μm/sec. Based on these observations, it has been proposed that peristaltic motion of the arterial wall generates a "pumping" force that drives the net flow of CSF parallel to the direction of the pulse wave propagation.

In this study, we apply the well-established fluid dynamic principles of peristalsis to study the nature of fluid flow in the PVS, aiming to bridge the gap between experimental observations and hypotheses. As previous studies of CSF flow in the PVS disagree on both the direction and the flow rates[8–10], we started our calculations by revisiting the mechanism of peristaltic pumping using time-dependent fluid dynamic simulations with fluid particle tracking in a deforming domain. By emphasizing the mechanism of peristatic pumping, we aimed at providing a clear physical interpretation for our calculations. We then performed fluid dynamic simulations on more realistic models of the PVS. Our simulations suggest that peristalsis with physiologically-plausible pulsation cannot drive the experimentally-observed fluid flow. However, we found that a small, constant pressure gradient

[1]Department of Engineering Science and Mechanics, The Pennsylvania State University, University Park, PA, United States. [2]Center for Neural Engineering, The Pennsylvania State University, University Park, PA, United States. [3]Department of Biomedical Engineering, The Pennsylvania State University, University Park, PA, United States. [4]Department of Neurosurgery, The Pennsylvania State University, University Park, PA, United States. [5]Department of Mathematics, The Pennsylvania State University, University Park, PA, United States. ✉e-mail: fxc8@psu.edu
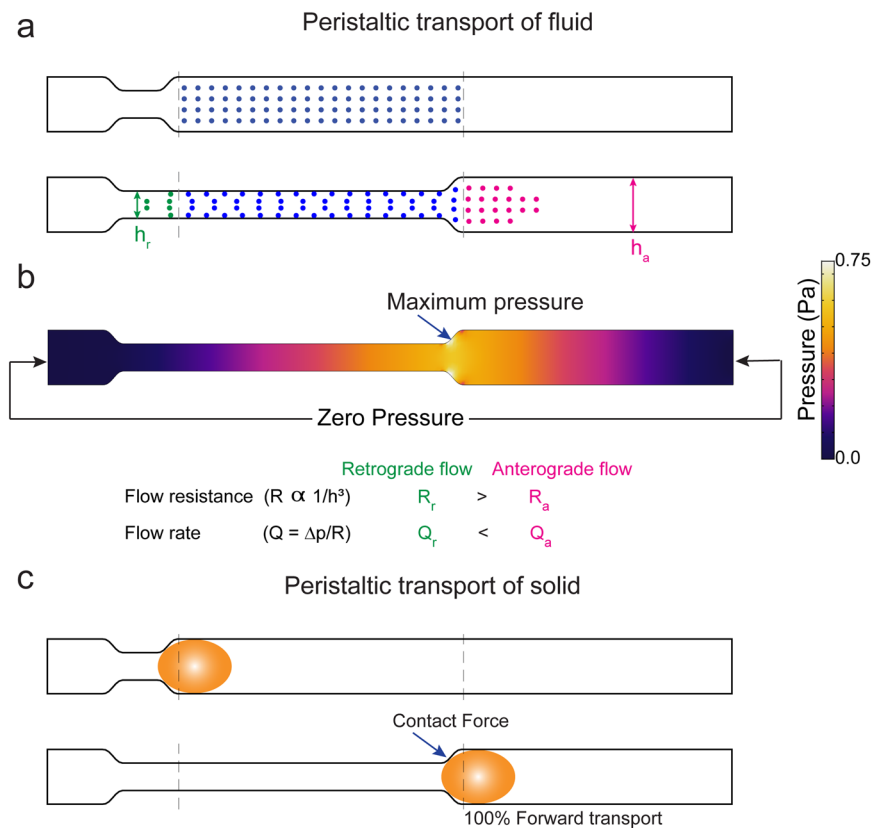
Figure 1. Mechanism of forward transport (pumping) driven by peristalsis in fluids and solids. (**a**) The movement of fluid (the dots represent fluid particles) driven by peristaltic compression of the walls of a 2D tube. The fluid movement in this figure is calculated using the Navier-Stokes equation with zero traction (pressure) at the two ends of the tube. (**b**) The pressure field in the tube in the deformed state. The fluid is displaced by the moving walls and this creates high pressure at the neck of wall movement. The pressure difference is same for retrograde and anterograde flow. However, the resistance is large posterior to the site of contraction. Compared to anterograde flow, retrograde flow needs the fluid to flow through a narrower tube. This results in a greater anterograde flow (magenta dots in **a**) compared to retrograde flow (green dots in **a**). (**c**) The movement of a solid bolus (yellow ellipse) driven by peristaltic motion of the walls of a 2D tube. The contact forces between the moving walls and the solid bolus are responsible for forward transport. The position of the solid bolus with respect to the dotted lines shows that the solid is moved forward. (**a**) was generated with MATLAB 2019b(https://www.mathworks.com/products/matlab.html). (**b**) was generated with COMSOL Multiphysics 5.4 (http://comsol.com). (**c**) was drawn in Adobe Illustrator 23.0(https://www.adobe.com/products/illustrator.html).

(of order 0.01 mmHg/mm) can account for the net forward movement observed experimentally. These results suggest that the observed directional movement of CSF in the PVS is generated by naturally occurring and/or experimenter-generated pressure differences, but not by arterial pulsations.

Results

We first examine how peristaltic motion affects the flow of an incompressible fluid in a two-dimensional tube. Consider a fluid-filled tube with deformable walls and no pressure difference across its two ends. When the position of the walls is fixed, there is no pressure gradient, and therefore no fluid flow (Fig. 1a,b). When the walls move inward due to a peristaltic wave propagating to the right (Fig. 1a), the fluid-filled domain deforms and the fluid is displaced. When the direction of the fluid flow is the same as the peristaltic wave, the motion is said to be anterograde – otherwise it is said to be retrograde. The flow in both directions is a result of the fluid pressure distribution, shown in Fig. 1b. The pressure is maximum at the location of the moving neck and is minimum at the two ends of the tube. Therefore, the fluid that is displaced by the wall is subject to the same pressure difference (Δp) in either direction ($\Delta p_a = \Delta p_r$, where the subscripts 'a' and 'r' denote the anterograde and retrograde flows, respectively). However, since the width of the tube (h) is smaller in one direction ($h_a > h_r$), there is more resistance for retrograde flow than anterograde flow (since flow resistance R scales with width of the tube $R \propto 1/h^3$ for 2D flow, $R_a < R_r$). As a result of this difference in flow resistance, the anterograde flow is greater than the retrograde flow (flow rate, $Q = \Delta p/R$, $Q_a > Q_r$). Thus, while peristalsis drives both anterograde and retrograde flows, a net flow in the direction of the peristaltic wave emerges (Video SV1). This example is a simplified version of peristalsis, where, the walls of the fluid-filled tube only contract. An example with a periodic contraction and expansion of the walls is demonstrated in Fig. S1 and Video SV2.
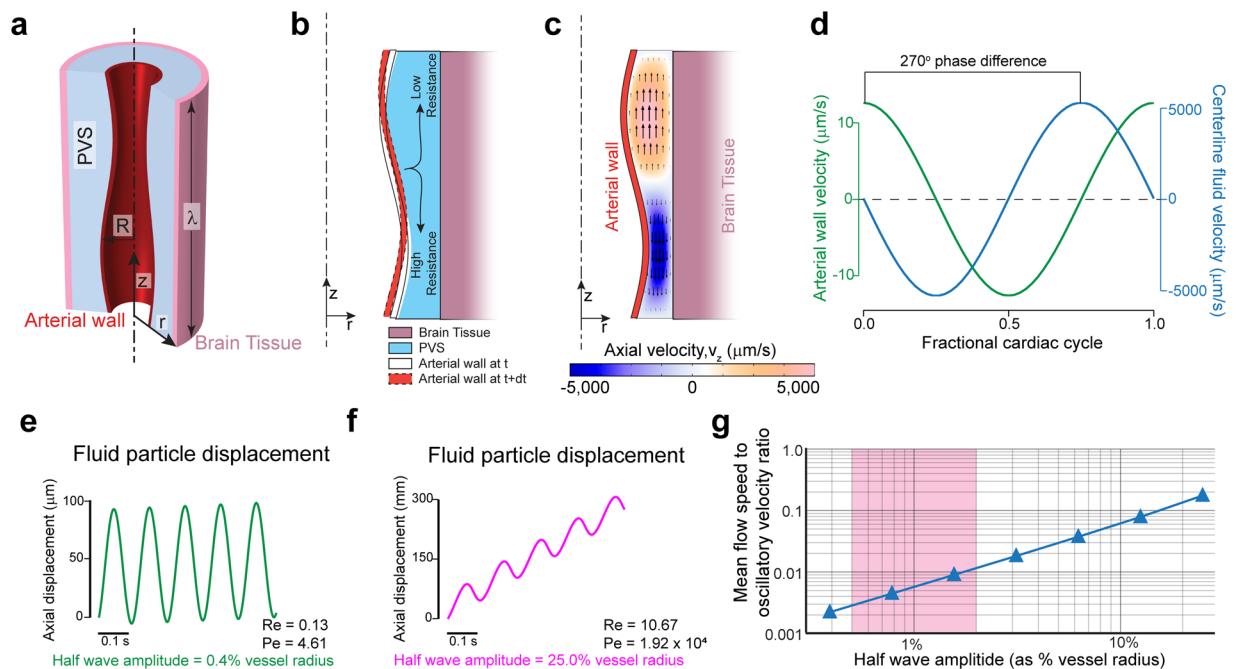
Figure 2. Heartrate pulsations drive oscillatory, but not directional flow. Large non-physiological pulsations are required for appreciable peristaltic pumping. (**a**) Schematic of the axisymmetric peristatic pumping model. The arterial wall undergoes peristatic movement, while the outer wall of the PVS is fixed. The length of the PVS is taken as one wavelength of the peristaltic wave (λ) with periodic boundary conditions at the two axial ends. (**b**) Schematic of the fluid motion during periodic peristalsis. The fluid displaced by the moving wall should move with lower resistance along the direction of the peristaltic wave than in the opposite direction. This difference in flow resistance results in net forward pumping. (**c**) The magnitude of the axial velocity is denoted by color, with arrows showing the direction. The half-wave amplitude of the peristaltic wave is 0.8% of the vessel radius. The deformations are scaled by a factor of 50 in the figure to clearly show the arterial wall movement. (**d**) The plots show the relative phase between arterial wall velocity and the centerline fluid velocity at the same axial (z) location (midpoint, $z = \lambda/2$). There is a 270° phase difference between the wall velocity and fluid velocity. (**e**) The trajectory (in z) of a fluid particle at the center of the PVS, where the amplitude of the peristaltic wave is similar to heartbeat driven pulsation[6,7] (0.8% peak-to-peak change in arterial radius). The flow is mostly oscillatory with very little unidirectional movement. (**f**) The trajectory (in z) of a fluid particle at the center of the PVS, where the amplitude of the peristaltic wave is unrealistically large (50% peak-to-peak change in arterial radius). This trajectory with appreciable unidirectional movement looks similar to experimental results[6,7]. (**g**) Plot showing the ratio of mean flow speed (average unidirectional flow velocity) to oscillatory velocity (peak velocity change in a cycle) as a function of the amplitude of the peristaltic wave. The shaded region shows the normal amplitude of pulsation cerebral arteries (1–4% of arterial radius peak-to-peak). Note that in this range, the oscillatory velocity is ~2 orders of magnitude higher than the pumping velocity (**a–d**). were generated with COMSOL Multiphysics 5.4(http://comsol.com). (**e–g**) were generated with MATLAB 2019b(https://www.mathworks.com/products/matlab.html).

It is important to bear in mind the difference between peristaltic transport of fluids and peristatic transport of solids. The textbook picture of peristalsis[22,23] is derived from the transport of solid matter in the esophagus and the gastro-intestinal tract. When solid matter is transported by peristalsis, all of the material moves in the direction of the peristaltic wave (Fig. 1c). This differs from the case of fluid transport by peristalsis, which generates both anterograde and retrograde flows (Figs. 1b, S1). Moreover, the peristaltic transport of solids is independent of the magnitude of wall motion and the length of the tube. In contrast, the nature of fluid flow in a tube driven by peristaltic motion of the walls is highly depended on the magnitude of both wall motion and tube length[24], which we will demonstrate in the results. This understanding of the mechanism of peristaltic transport of fluids is crucial to interpreting the results of fluid dynamic models of the PVS. The assumptions of the shape, size and the deformation of the PVS may vary between the models, but the mechanism of peristaltic transport remains the same.

Peristaltic pumping requires unphysiologically large amplitude pulsations for meaningful fluid flows. To understand the relation between arterial wall movement and fluid movement in the PVS, we created a model of peristaltic pumping. In our model, the geometry of the PVS is taken to be cylindrically symmetric, with the artery centered within the PVS (Fig. 2a). While the geometry of the fluid domain is simplified, the inner and outer radii are based on realistic values (see methods). We then imposed a sinusoidal peristaltic wave on the arterial wall, while keeping the outer wall of the PVS fixed, effectively making the brain tissue rigid. In order to capture the whole peristaltic wave, the length of the PVS used in the simulation was equal to one wavelength (λ)

of the peristaltic wave (see methods). Since we are interested in studying the pumping generated by arterial wall movement alone, we used periodic boundary conditions at the axial ends of the PVS. This is equivalent to studying flow driven by peristalsis with no additional pressure differences[8,14,15,25]. We tracked the motion of particles at the center of the PVS.

Peristaltic pumping of fluid is a result of lower flow resistance for anterograde flow and higher resistance for retrograde flow (see Figs. 1 and 2b). This explains the fluid velocities observed with respect to the arterial wall position and wall velocity (Fig. 2c,d). The phase difference between the arterial wall velocity and the downstream fluid velocity (axial velocity, v_z) remained the same throughout the length of the domain. Flow resistance (R_{flow}) of a tube with an annular cross-section decreases with approximately the fourth power of the internal radius[26]. For slow, laminar flows like those in the paravascular space, the flow resistance of a tube with annular cross-section is given by the equation:

$$Q = \frac{-\partial p/\partial z}{R_{flow}}; R_{flow} = \frac{8\mu}{\pi}\left[r_2^4 - r_1^4 - \frac{(r_2^2 - r_1^2)^2}{ln(r_2/r_1)}\right]^{-1}$$

(1)

Where Q is the flow rate, p is the pressure and μ is the dynamic viscosity of the fluid. The internal and external radii of the annular region are given by r_1 and r_2 respectively. For our calculations, Reynolds numbers range from 0.13 to 10.67, well within the laminar flow regime. Given the strong dependence of fluid resistance on the diameter, it follows that the amplitude of pulsations (the change in internal radius) should have a large effect on the flow resistance changes and therefore the pumping generated by peristaltic motion.

We examined the relation between pulsation amplitude and the trajectory of the fluid particles in the PVS. To put our results in the context of experimental findings, the typical half wave amplitude of heartbeat pulsations is 0.5–2% of arterial diameter[6,7]. Our simulations show that such small amplitude pulsations generate little difference between forward and backward flow resistance, which resulted in oscillatory fluid flow with minimal net anterograde flow (Fig. 2e). However, the kind of fluid particle trajectories reported by Bedussi et al.[6] and Mestre et al.[7] are very different from the ones simulated in Fig. 2e. The fluid trajectories in the PVS observed in both studies are more similar to the ones shown in Fig. 2f, where the net anterograde motion of the fluid is of the same order as the oscillatory motion. Sample CSF particles trajectories can be found in the supplementary videos of Mestre et al.[7] and Fig. 3 of Bedussi et al.[6]. This kind of fluid motion would require non-physiological amplitudes arterial pulsations, with half wave amplitudes around 25% of the arterial radius. To better understand the effect of pulsation amplitude on fluid flow, we examined the relation between the pulsation amplitude and the ratio of mean flow speed (or average anterograde velocity) to oscillatory velocity (difference between peak anterograde velocity to peak retrograde velocity) (Fig. 2g). Measurements by Mestre et al.[7] show that mean flow speed (~20 μm/s) and oscillatory velocity (~10 μm/s) are of the same order. Our simulations show that for heartbeat-driven pulsations (1–4% of arterial radius peak-to-peak[6,7,27]), the mean flow speed is 2–3 orders of magnitude smaller than the oscillatory velocity (Fig. 2g). These result show that heartbeat-driven pulsations in an idealized model are too small to explain the directed flow of CSF seen in vivo.

While the shape of the PVS in our model was simplified, the model still provides important generalizable insights into the mechanism of peristalsis. Specifically, the model helps us understand the relation between the movement of the arterial wall and the flow of fluid. We found that the radial wall velocity and the anterograde fluid velocity are always out of phase (by 270°, Fig. 2c,d), and that the kind of fluid trajectories observed in vivo would require large, non-physiological amplitudes for arterial pulsations. Next, we examined if these results held for a 3-dimensional model of peristalsis with a realistically shaped PVS and pulse waveform.

Paravascular flow measurements are inconsistent with peristaltic pumping. To test if fluid flow is influenced by the details of the shape of the PVS or the waveform of heartbeat driven pulsations, we created a model with a realistically-sized and shaped PVS, with a cardiac waveform drawn from experimental data[7] (Fig. 3a,b). The outer wall of the PVS was assumed to be fixed, and the length of the domain was set to be equal to one wavelength (λ) of the peristaltic wave. We use a no pressure (traction) boundary condition at the boundaries in place of the periodic boundary condition used for the axisymmetric simulations. This is done to better estimate the pressure changes in the PVS (Fig. 3e).

The mean flow speed (anterograde velocity time-averaged over a complete cycle) of fluid particles at the centerline of the PVS in our simulation was 102.1 μm/s. However, this was accompanied by oscillatory fluid velocities of approximately 30,000 μm/sec, well over a hundred times the mean flow speed (Fig. 3c,d). The simulations also show the phase relation between the arterial wall velocity (radial component of wall velocity) and the fluid anterograde velocity (axial component of fluid velocity). It is clear that the wall velocity and the fluid velocity are out of phase, i.e., when the arterial wall dilates, the fluid flows in the retrograde direction and, when the arterial wall constricts, the fluid flows in the retrograde direction. This phase relation between the velocities is consistent with our axisymmetric model (Fig. 2d). This is in contrast to the in vivo measurements by both Bedussi et al.[6] and Mestre et al.[7] (Fig. 4d), where the fluid flows in phase with the arterial wall, i.e., when the artery dilates, the fluid flow is anterograde and vice versa. Viewed together with the results of the axisymmetric simulations, our simulations suggest that the shape of the PVS and the waveform of heartbeat pulsations cannot pump CSF in a model with a simplified geometry of the PVS.

These results show that a peristaltic pumping model is inconsistent with experimental findings, which suggests that there are some problems with the assumptions of the peristaltic pumping model. In the next section, we revisit these assumptions and attempt to match the results of the fluid dynamic calculations with experimental findings.
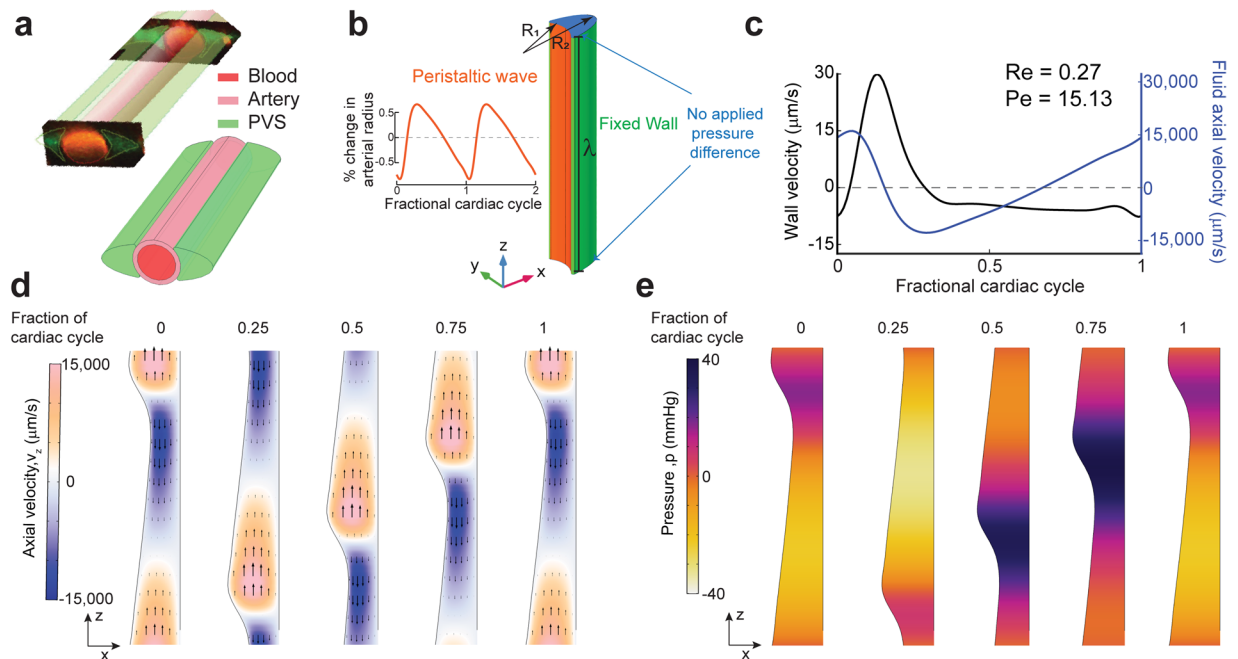
Figure 3. Simulations of arterial pulsations in a model with an elliptic PVS show that observed fluid flows are inconsistent with a peristaltic pumping mechanism. (**a**) The 3D geometry of the PVS used in our simulations replicates the PVS geometry observed *in vivo* in mice. The figure in top-left is taken from Mestre *et al.*[7] and the figure on the bottom-right shows the 3D geometry used in our calculations. (**b**) The dimensions and boundary conditions used in 3D fluid dynamics simulations. The wall movement on the arterial side (orange) is given by a travelling wave with a realistic waveform observed *in vivo* in mice[7] (inset). The wall on the brain tissue side is fixed (green). The parameters (R_1, R_2, λetc are given in Table 1). (**c**) Plots showing the arterial wall velocity and the centerline velocity of the fluid taken at the same axial (z) location. While the wall velocity profile and magnitude are very similar to what was observed *in vivo*[7], the oscillatory fluid velocity is ~1000x higher than the values observed *in vivo*[6,7]. Moreover, the peak fluid velocity is not in phase with the wall velocity. These discrepancies were predicted by our simplified model (Fig. 2). (**d**) The colors show axial velocity profile at the mid-section of the PVS (XZ plane at y = 0) throughout the cardiac cycle. Arrows are provided to make the interpretation of flow easier. The fluid velocity profile agrees with our expectations from the mechanism of peristalsis (Fig. 2b) and our simplified model (Fig. 2c). The deformations are increased by a factor of 50 in post-processing to clearly show the arterial wall movement. (**e**) Corresponding pressure profile at the mid-section of the PVS (XZ plane at y = 0) throughout the cardiac cycle. The deformations are scaled by a factor of 50 in post-processing to clearly show the arterial wall movement. All the subplots were generated with COMSOL Multiphysics 5.4(http://comsol.com), with the exception of the top left image in a (citation provided).

Parameter Name	Symbol	Value	Unit	Source
Arterial radius	R_1	30	μm	[7]
PVS width	wd	40	μm	[7]
PVS outer radius	R_2	70	μm	R_1 + wd
CSF viscosity	μ_f	0.001	Pa.s	[79,80]
CSF Density	ρ_f	1000	kg/m³	[79,80]
Pulsation Frequency	f	8.67	Hz	[7]
Pulse wave speed	c	1	m/s	[27,28]
Pulse wave wavelength	λ	0.12	m	c/f
MCA Length	L_a	5	mm	[6,32,33]
Diffusion coefficient	D	1.4×10^{-6}	cm²/s	[81,82]

Table 1. Parameters used in simulations.

Pressure differences, not arterial pulsations drive bulk fluid flow.

In order to better capture the geometry of the PVS, we made changes to our 3D model based on the anatomy of the brain, the subarachnoid space and cerebral vasculature. We shortened the length of the PVS to 5 mm, and made the outer wall of the PVS move with the pulsations. Previous peristaltic pumping models[8,9,14,15] have set the length of the fluid chamber to be equal to one wavelength of the peristaltic wave. However, the wavelength of the peristaltic motion of arteries is considerably larger than the length of the middle cerebral artery (MCA), the proposed source of peristaltic
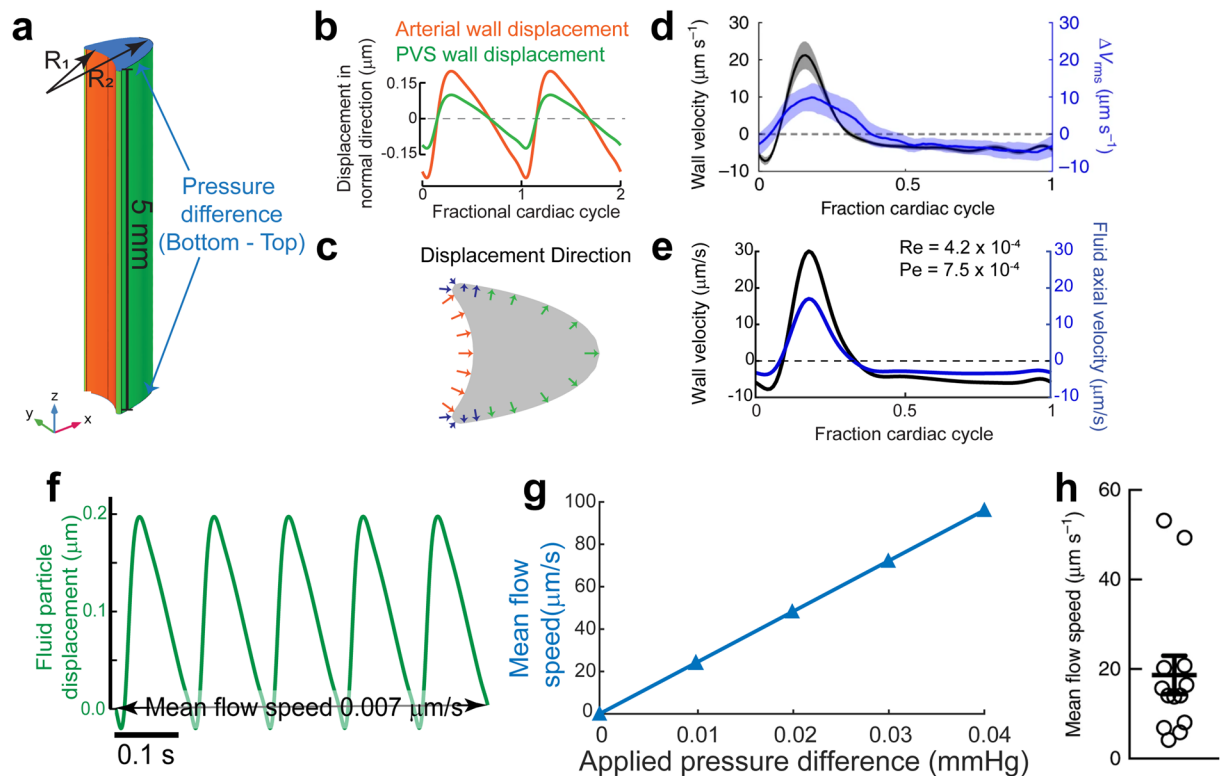
Figure 4. A small, constant pressure gradient can explain directed fluid movement *in vivo*. (**a**) Schematic of the model. The length of the PVS is set to 5 mm to match the length of the MCA in mice (4–6mm[6,32,33]). An additional pressure difference between the inlet and outlet is applied. (**b**) The displacement of the arterial wall (orange) and the PVS wall (green) used in the simulation. The displacement is given in the direction of the surface normals shown in (**c**). (**c**) Positive displacement direction at a cross-section of the PVS, this is the direction of displacement for the plots shown in (**b**) The Inner wall is shown in orange and the outer wall is shown in green. The displacement changes in amplitude and direction from the inner wall to the outer wall. This transition is carried out using the smooth, step function in COMSOL Multiphysics. The changing direction and length of the blue arrows indicates the smooth transition. (**d**) Plot showing arterial wall velocity and oscillations in fluid velocity measured *in vivo*. Adapted from Mestre *et al.*[7] (**e**) Plot showing arterial wall velocity and oscillations in downstream fluid velocity our simulation matches with those in (**d**). (**f**) Plot of the trajectory of a fluid particle in the z direction shows that there is very little pumping by arterial wall movement. (**g**) Plot showing the relation between an applied pressure difference across the ends of the PVS and the mean anterograde flow speed. An additional 0.01 mmHg pressure difference across the PVS is required to achieve a mean flow speed of 24.4 μm/s, similar to the mean flow speeds observed *in vivo* (**h**). (**h**) Mean flow speed in the PVS measured *in vivo*. Adapted from Mestre *et al.*[7] (**a–c,e**). were generated with COMSOL Multiphysics 5.4 (http://comsol.com). (**f,g**) were generated using MATLAB 2019b (https://www.mathworks.com/products/matlab.html).

pumping. With a peristaltic wave speed of 0.5–2 m/s[27,28], and a heartbeat frequency of 6–10 beats/second in mice[6,7,29–31], the wavelength of the peristaltic wave is between 50–160 mm in mice, while the MCA is only 4–6 mm long in mice[6,32,33]. This means that the pulse wave travels so fast across the length of the PVS that the arterial wall moves in and out simultaneously and therefore there is no appreciable difference in the flow resistance for anterograde and retrograde flows (Fig. S2). We calculated the fluid particle trajectories 1 mm from the distal end of the PVS segment (z = 4 mm), which captures the geometry of the surface of the brain where the flow measurements were made. This corrected the inconsistency between the phase of the fluid downstream velocity and the arterial wall velocity found in the peristaltic pumping model with a length of one pulsation wavelength (Fig. S2). Our results are similar to the phase relation between arterial wall velocity and fluid velocity estimated by Asgari *et al.*[10], who studied the flow driven by penetrating arterioles in a model with anatomically realistic dimensions.

Secondly, the fixing of the outer wall of the PVS in other models means that the brain tissue and the subarachnoid space that surround the PVS are rigid. This is not realistic because the brain tissue is very soft, with a shear modulus in the range of 1–8 kPa[34–38] (7.5–60 mmHg) and the 80 mmHg pressure changes (Fig. 3e) predicted by the peristaltic pumping model will cause substantial deformations. To include the effect of the soft tissue, we moved outer wall of the PVS with the same frequency as the heartbeat driven pulsations (Fig. 4b). We applied these small, pressure-driven deformations in the direction of the outward normal of the surface of the PVS, because pressure-like forces act along the outward normal of a surface. Since the mechanical properties of the

subarachnoid space are mostly unknown[39–42], we adjusted the amplitude of these deformations so that the oscillatory fluid velocity matched that observed *in vivo* by Mestre *et al.*[7].

Our simulations suggest that the wall movement itself can only drive oscillations in fluid flow with negligible (0.007 μm/s) mean anterograde flow. The time course of fluid velocity from our simulations and its relation to the arterial wall movement agrees very well with the measured values in both phase and magnitude (Fig. 4d,e). The phase relation between the arterial wall velocity and the fluid velocity is a direct result of correcting the length of the PVS, while the magnitude of fluid velocity is corrected by including movement of the outer walls of the PVS in the simulation. However, the simulations suggest that arterial pulsations generate very little net anterograde flow with a time averaged downstream velocity of 0.007 μm/s (Fig. 4f).

Finally, we tested the possibility that small pressure differences across the ends of the PVS can drive the bulk flow observed in the experimental studies. We calculated the fluid flow through the PVS while varying the imposed pressure difference over a physiologically plausible range. We found that a very small pressure difference, 0.01 mmHg across the length of the PVS (5 mm), was sufficient to drive a mean downstream speed of 24.4 μm/sec (Fig. 4g), close to the mean flow speed observed *in vivo*[7] (Fig. 4h). The pressure difference value was also found using equations derived in another recent theoretical study that estimated the flow resistance of paravascular spaces[26]. Such a small pressure difference is practically impossible to measure in live animals, due to the lack of instruments sensitive to such small changes[43,44]. The pressure differences could be normally present due to CSF production in the ventricles[43] and drainage via meningeal lymphatic vessels[45,46] and the cribriform plate[47], or be generated by intracranial injections[48,49] of the tracer spheres. We conclude that peristalsis cannot drive unidirectional fluid pumping in the PVS of cerebral arteries under physiological conditions and that the experimentally observed CSF flow in the PVS is probably due to pressure differences present in the system.

Discussion

Peristaltic pumping has been hypothesized to drive directed movement of cerebrospinal fluid in the paravascular space. In this study we test the "peristaltic pumping" hypothesis, by using simulations of fluid dynamics to understand what experimental measurements tell us about bulk flow. We started with simple models to provide a physical interpretation to the process of peristalsis of fluids and built more physiologically realistic models informed by the results of these models. We were able to improve upon previously published computational models aimed at studying the flow of CSF in the PVS[8–10,25], using the detailed anatomical and physiological information from the experiments by Mestre *et al.*[7]. This experimental data provided information about the shape of the PVS around cerebral arteries and the amplitude and waveform of the heartbeat driven pulsations, which we used in our modeling. The experiments also had detailed information on the oscillatory and anterograde flow of CSF in the PVS. Our simulations show that the cardiac pulsation of arteries is only capable of driving the oscillatory motion of CSF in the PVS, and not the unidirectional bulk flow. Rather, the experimentally observed unidirectional flow is likely to be driven by pressure differences in the system.

Our simulations point to two main reasons why arterial pulsations cannot drive unidirectional fluid flow in the PVS. First, direct measurement of cortical arteriole diameters in mice using two-photon imaging shows that the amplitude of the heartbeat-driven pulsations is small (1–4% peak to peak change in arterial diameter[6,50,51]). In humans, CT angiography has shown that pulsations drive only a maximum of 4–6%[52,53] change in the volume of the MCA (2–3% change in diameter assuming a cylindrical geometry). Our calculations show that substantially larger cardiac pulsations (roughly 50% peak-to-peak change in diameter) are required to drive significant directed motion of the fluid relative to the oscillatory motion. Second, the peristaltic motion of arteries cannot drive unidirectional fluid flow because the length of the PVS is substantially less than the wavelength of the peristaltic wave. The total length of the MCA is between 4–6 mm in mice[6,32,33], while the wavelength of the peristaltic wave is between 100–1000 mm (based on the pulse wave velocity of 1–5 m/s[27,28] and a heart rate of 6–12 Hz[29,30]). This is over an order of magnitude difference between the length of the PVS and the wavelength of the peristaltic wave. In humans, the MCA is longer, (roughly 100 mm [54]). However, while the pulse wave velocity, a function of arterial stiffness[55,56], remains roughly the same in mice and humans[57,58], the heartrate in humans is around 1–2 Hz, which makes the wavelength of the peristaltic wave 1–2 orders of magnitude higher than the length of the MCA in humans. Therefore, in mice as well as in humans, arterial pulsations are unlikely to drive unidirectional CSF flow. While arterial pulsations cannot cause directed flow in the PVS, it is possible that these pulsations improve metabolite transport in the brain through dispersion. Asgari *et al.*[10] showed that dispersion could be a mechanism of transport in the PVS surrounding penetrating arteries in the absence of directed flow. Sharp *et al.*[59] showed that oscillatory flow could result in faster metabolite transport compared to diffusion in the periarterial, paraarterial and the spinal subarachnoid space.

The model assumes that there is no inherent preference to directional flow in the PVS and that any flow in the PVS is a direct result of pressure differences and incompressibility of CSF (fluid continuity equation). It is however possible that the PVS or other fluid-filled chambers in the cranial space could contain valve-like structures that are responsible for a directional preference for flow. Valve like structures are present in the lymphatic vessels[60], veins[61] and arachnoid granulations[62,63] in mammals. To the best of our knowledge, no such valve-like have been observed in the PVS. Moreover, Mestre *et al.*[7] showed that retrograde flow of CSF is observed during hypertension, which suggests that valve-like structures are either absent in the PVS or that these structures are impaired during hypertension.

Based on the experimental evidence available, we speculate that two possible mechanisms that could generate pressure differences to drive directional CSF flow in the PVS, namely, CSF production in the choroid plexus and osmotic pressure differences across astrocytic end feet. CSF flow through the PVS and into the brain is severely affected in aquaporin-4 (AQP4) knockout mice[1,50]. The AQP4 channel is selectively permeable to water[64,65] and is present in the choroid plexus[66] and the astrocytic endfeet[1]. The deletion of the AQP4 gene could reduce CSF production and osmotic flow through astrocytic endfeet. It is possible that a combination of the two factors drive CSF

flow since the osmotic concentration gradients and the CSF production rate are interrelated[67]. Alternatively, the observed flow in the PVS might be an caused by the infusion rate of 1–2 μl/min used in the experiments to study CSF flow[6,7], which is 3–5 times the typical rate of CSF production rate in mice (0.38 μl/min[43]). The infusion rate used in these experiments is known to increase intercranial pressure[1,44], as pointed out by Hladky and Barrand[48]. A detailed 3-D model of the whole brain with the PVS and the SAS, all modelled as poroelastic media[68] would be needed to test the possibility of the observed flow being an artifact of the infusion.

An important result of our simulations is that the paravascular spaces around pial arterioles provide a crucial pathway for fluid transport in the brain due to their low flow resistance. A very small pressure difference (0.01 mmHg, Fig. 4g) across the length of the MCA (5 mm) can be sufficient to drive fluid through the PVS with a mean speed of ~20 μm/s. This pressure difference is equivalent to a pressure gradient of 2 mmHg/m, which is very close to the pressure gradient of 2.85 mmHg/m[69] between the ventricular and subdural space measured in humans. This is in stark contrast to the much less permeable brain tissue, where a pressure gradient of 1 mmHg/mm can only generate fluid velocities in the order of 0.010 μm/s[70]. However, the low flow resistance makes understanding the driving force for CSF movement in the PVS extremely difficult. A pressure difference in the range of 0.01 mmHg cannot be accurately measured with current instruments, which have a resolution of around 1 mmHg[43,71]. Moreover, invasive access of the skull probes through the skull severely affects the flow through the PVS[50].

Methods

Model equations and boundary conditions.
We use a standard time-dependent finite element method to solve the equations of fluid motion in the PVS. These equations are formulated to correctly account for the deformation of the PVS. Specifically, we write the equations in Arbitrary Lagrangian-Eulerian (ALE) coordinates (see appendix). As is well-known, ALE formulations are able to account for the deformation of the solution's domain at the expense of having to determine an auxiliary motion typically referred to as the "mesh motion"[72–74]. The governing equations for the fluid and the mesh movement are written in their weak, tensor form (see Appendix) and converted to their component form using Wolfram Mathematica. These component form equations are implemented in COMSOL Multiphysics (Burlington, MA) using the "Weak Form PDE" interface, where PDE stands for partial differential equation. Therefore, the overall solution scheme is our own, and COMSOL Multiphysics simply provides a high-level integrated programming environment within which said scheme is implemented.

The fluid (CSF) velocity and pressure are governed by the incompressible Navier-Stokes equations (Eqs. 1–3). We solve for the fluid velocity (v_f) and pressure (p_f) in the PVS as a function of time (t). In Eq. 1, ρ_f and σ_f are the fluid's mass density and Cauchy stress, respectively. In Eq. 3, μ_f is the fluid's dynamic viscosity.

$$\frac{\partial v_f}{\partial t} + (v_f . \nabla)v_f - \frac{1}{\rho_f}\nabla \cdot \sigma_f = 0 \tag{1}$$

$$\nabla . v_f = 0 \tag{2}$$

$$\sigma_f = -p_f I + \mu_f(\nabla v_f + (\nabla v_f)^T) \tag{3}$$

The governing equation for the mesh motion is dictated by convenience and, where necessary, by the problem's geometric constraints. In our problem, the deformation of the solution's domain (PVS) is relatively mild and therefore we the mesh motion equation, with primary unknown given by the mesh displacement u_m, is chosen to be a linear elliptic model[75], namely the Laplace equation (Eq. 4):

$$\nabla . (\nabla u_m) = 0 \tag{4}$$

We use no-slip boundary condition at the inner and outer walls of the PVS, *i.e.*, fluid velocity is equal to the wall velocity in all simulations (Eq. 5). For the axisymmetric simulations, the inner walls have a baseline radius of R_1 and the outer walls have a fixed radius of R_2. The movement of the inner walls is given by a travelling sinusoidal wave (Eq. 6). There is no wall movement at the outer wall (Eq. 7). The total length of the tube is taken equal to the wavelength (λ) of the peristaltic wave. Periodic boundary conditions are used at the two ends of the tube (Eq. 8). To obtain a unique pressure solution, a global constrain is applied for the total pressure (Eq. 9).

$$\text{at } r = R_1 \text{ and } r = R_2, \ v_f = \frac{\partial u_m}{\partial t} \tag{5}$$

$$\text{at } r = R_1, \ u_{mr} = \varnothing R_1 Sin\left[\frac{2\pi}{\lambda}(z - ct)\right], \ u_{mz} = 0 \tag{6}$$

$$\text{at } r = R_2, \ u_{mr} = 0, \ u_{mz} = 0 \tag{7}$$

$$v_f\Big|_{z=0} = v_f\Big|_{z=\lambda}; \ p_f\Big|_{z=0} = p_f\Big|_{z=\lambda} \tag{8}$$

$$\int p_f = 0 \tag{9}$$

In Eqs. 6,7, u_{mr} and u_{mz} are the r and z components of the mesh displacement (u_m). $\varnothing$ is the half wave amplitude of the peristaltic wave, as a fraction of the baseline diameter R_1. c is the speed of the peristaltic wave. The integration in Eq. 9 is performed over the entire computational domain.

For the 3D simulations presented in Figs. 3 and 4, we created the cross section of the PVS to resemble the geometries observed *in vivo*[7,26]. The inner wall of the cross section is a circle of radius R_1. The outer wall of the cross section is an ellipse with major axis R_2 and minor axis $0.8R_1$. The intersection of the circle with the ellipse is smoothened with a fillet of radius $0.08R1$. The cross-section can be divided into three regions. The three regions can be identified in Fig. 4c. The inner walls of the PVS (the walls facing the arteries or the circular face) are shown in orange. At the inner walls, a dilation of the arterial wall will cause a deformation of the PVS in the direction opposite to the unit outward normal, n (Eq. 10). The outer walls of the PVS (wall facing the SAS or the brain tissue or the elliptical face) are shown with green arrows in Fig. 4c. On the outer walls, the pressure is higher when the vessel dilates and lower when the vessel contracts (Fig. 3e). Therefore, when the vessel dilates, the outer walls of the PVS deform in the direction of the outward normal, n (Eq. 11). We call the part of the wall between these two regions, the transition region (the fillet region shown with blue arrows in Fig. 4c). Here, the displacement is smoothly transitioned using the step function available in COMSOL Multiphysics.

$$\text{at inner walls: } u_m = -an[ct - z]n \tag{10}$$

$$\text{at outer walls: } u_m = \varphi\, an[ct - z]n \tag{11}$$

In Eqs. 10 and 11, 'an' is a periodic function with a time period of 1/f, where f is the heartrate frequency. The waveform of '*an*' is interpolated from the pulsation waveform reported by Mestre *et al.*[7] (Figs. 3b, 4b). The value of φ (SAS displacement parameter) is 0 for the simulations presented in Fig. 3 and Fig S2. For the simulations presented in Fig. 4, the value of φ is 0.368.

For the simulations shown in Fig. 3, no traction was applied at the axial ends of the PVS (Eqs. 12,13). This change was useful to understand the magnitude of pressure changes in the PVS (Fig. 3e).

$$\text{at } z = 0,\ \sigma_f.\ n = 0 \tag{12}$$

$$\text{at } z = \lambda,\ \sigma_f.\ n = 0 \tag{13}$$

For the simulations shown in Fig. 4, no traction is applied at the distal end of the PVS ($z = L_a$, where L_a is the length of the MCA). This is similar to Eq. 13. At the proximal end, a pressure like traction is applied (Eq.14). The parameter p_1 in Eq. 14 is the pressure difference across the length of the PVS, shown on the x-axis of Fig. 4g. On the peripheral walls of the PVS, the fluid velocity is equal to the wall velocity (similar to Eq. 5).

$$\text{at } z = 0,\ \sigma_f.\ n = -p_1 n \tag{14}$$

The Reynolds number for all the simulations is calculated using the formula for flow in a pipe (Eq. 15). In Eq. 15, D_h is the hydraulic diameter, which is calculated using the area A and the perimeter P. Q is the flow rate. The Péclet number is calculated using the diffusion (D) coefficient for Amyloid-beta in water (Eq. 16). v_{ave} is the mean downstream speed of the fluid at the center of the PVS ($r = (R_1 + R_2)/2$).

$$Re = \frac{\rho_f\, Q\, D_h}{\mu\, A},\ D_h = 4A/P \tag{15}$$

$$Pe = \frac{v_{ave} D_h}{D} \tag{16}$$

The details about particle tracking in ALE are explained in the appendix. The particle tracking calculations and movies were made using MATLAB code. All the code for Wolfram Mathematica, COMSOL Multiphysics, and MATLAB are available to download on Github (https://github.com/DrewLab/Peristaltic-pumping-of-CSF.git).

Anisotropic non-dimensionalization. One of the major concerns when using finite element simulations to study flow in the PVS is the long and narrow geometry of the PVS. For example, the domain used for simulations presented in Fig. 2 has a length of one wavelength of the peristaltic wave (116.7 mm or 116,667 μm), which is nearly 3000 times the width of the PVS (40 μm). Simulating the geometry with these dimensions could cause a large number of elements, making it incredibly expensively to solve or create elements with very bad aspect ratios. To deal with this problem, we non-dimensionalized the equations with different scaling factors in the x, y (or r for axisymmetric simulations), and z directions. All the equations from the mesh coordinates (X_m) are rewritten in these non-dimensional coordinates (X_c) (Eq. 17). In Eq. 17, the coordinates are written in the conventional order, i.e, (x, y, z) for Cartesian and (r, θ, z) for cylindrical coordinates.

$$X_m = L_o \begin{pmatrix} 1 & 0 & 0 \\ 0 & 1 & 0 \\ 0 & 0 & g_3 \end{pmatrix} X_c$$

(17)

The characteristic length, L_o, was chosen to be equal to the arterial wall radius (R_1). The scaling factor, g_3, was chosen so that the axial (z) length of the domain in the non-dimensionalized coordinates is 10. This resulted in a scaling factor (g_3) value of ~400 in all the simulations. To verify the validity of this choice of parameter, we plotted the z and r components of the velocity gradient in the mesh coordinates and non-dimensional coordinates (Fig. S3). In the mesh coordinates, the velocity gradients (for the radial and the axial component) were nearly three orders of magnitude higher in the radial direction compared to the axial direction. Our choice of scaling factor results in velocity gradients of similar magnitude, which means that for meshes of aspect ratio ~1 in the non-dimensionalized coordinates, the approximation and interpolation errors are rather contained (for low Reynold's number flows). A similar line of reasoning is used to minimize approximation and interpolation errors for anisotropic adaptive meshing for flow simulations[76–78].

Finite element implementation. The governing equations and traction boundary conditions were written in their weak form (see appendix, section E) and implemented using the "Weak Form PDE" interface in COMSOL Multiphysics (Burlington, MA). The mesh consisted of rectangular elements with second order Lagrange polynomials for fluid velocity (v_f) and mesh displacement (u_m) and first order Lagrange polynomials for fluid pressure (p_f).

The mesh used in the axisymmetric simulations had 10 elements in the radial direction and 100 elements in the axial direction, with a higher density at the inner and outer walls of the annular section representing the PVS (Fig. S4a). We chose the ratio of the number of elements so that the aspect ratio of the elements in the computational domain was nearly one. We started with a mesh with just 5 elements and 50 elements in the radial and axial direction respectively. Then we refined the mesh by a factor of 2 for each iteration of the mesh and calculated the relative L2 error norm in velocity and pressure for each refinement (Eqs. 18,19). The error magnitude is integrated over the whole domain. We estimated the error for the values of m = 1, 2, 4, 8. We found that for a value of m = 2, the error norms for both velocity and pressure were below 0.1% (Fig. S4b). Therefore, we performed all the axisymmetric simulations with 10 elements in the radial direction and 100 elements in the axial direction. For the 3D simulations, we kept the same number of elements axially and created a graded rectangular mesh in the XY plane (Fig. S4c). The models had 9,553 and 1,290,356 degrees of freedom for the axisymmetric and 3D calculations respectively.

$$L2Err_v = \frac{\int v_{f,Mh=m} - v_{f,Mh=2m}}{\int v_{f,Mh=2m}}$$

(18)

$$L2Err_p = \frac{\int \left| p_{f,Mh=m} - p_{f,Mh=2m} \right|}{\int \left| p_{f,Mh=2m} \right|}$$

(19)

The time stepping for the time-dependent problems was performed using the backward difference formula with minimum order set to 1 and maximum order set to 5. The default order of the backward difference formula in COMSOL Multiphysics is 2. The maximum time step was set to 1/1000th of the heartbeat cycle. The relative error norm calculated by changing the time step from 0.001/f to 0.0005/f (similar to Eqs. 18 and 19), where f is the heartbeat frequency, was less than 10^{-8}%.

Model parameters. All the parameters were taken to match the values observed *in vivo* in mice. The dimensions of the cross-section of the PVS and the pulsation waveform of the arteries were taken from Mestre *et al.*[7], to emulate their experimental results. All the parameters used in the model are listed in Table 1.

References

1. Iliff, J. J. *et al.* A Paravascular Pathway Facilitates CSF Flow Through the Brain Parenchyma and the Clearance of Interstitial Solutes, Including Amyloid. *Sci. Transl. Med.* **4**, 147ra111–147ra111 (2012).
2. Abbott, N. J. Evidence for bulk flow of brain interstitial fluid: Significance for physiology and pathology. *Neurochem. Int.* **45**, 545–552 (2004).
3. Abbott, N. J., Pizzo, M. E., Preston, J. E., Janigro, D. & Thorne, R. G. The role of brain barriers in fluid movement in the CNS: is there a 'glymphatic' system? *Acta Neuropathol.* **135**, 1–21 (2018).
4. Iliff, J. J. *et al.* Cerebral Arterial Pulsation Drives Paravascular CSF-Interstitial Fluid Exchange in the Murine Brain. *J. Neurosci.* **33**, 18190–18199 (2013).
5. Bedussi, B. *et al.* Paravascular channels, cisterns, and the subarachnoid space in the rat brain: A single compartment with preferential pathways. *J. Cereb. Blood Flow Metab.* **37**, 1374–1385 (2017).
6. Bedussi, B., Almasian, M., de Vos, J., VanBavel, E. & Bakker, E. N. Paravascular spaces at the brain surface: Low resistance pathways for cerebrospinal fluid flow. *J. Cereb. Blood Flow Metab.* 0271678X1773798, https://doi.org/10.1177/0271678X17737984 (2017).
7. Mestre, H. *et al.* Flow of cerebrospinal fluid is driven by arterial pulsations and is reduced in hypertension. *Nat. Commun.* **9**, 4878 (2018).

8. Wang, P. & Olbricht, W. L. Fluid mechanics in the perivascular space. *J. Theor. Biol.* **274**, 52–57 (2011).
9. Schley, D., Carare-Nnadi, R., Please, C. P., Perry, V. H. & Weller, R. O. Mechanisms to explain the reverse perivascular transport of solutes out of the brain. *J. Theor. Biol.* **238**, 962–974 (2006).
10. Asgari, M., De Zélicourt, D. & Kurtcuoglu, V. Glymphatic solute transport does not require bulk flow. *Sci. Rep.* **6**, 1–11 (2016).
11. Iliff, J. J. *et al.* Cerebral Arterial Pulsation Drives Paravascular CSF – Interstitial Fluid Exchange in the Murine Brain. *J. Neurosci.* **33**, 18190–18199 (2013).
12. Smith, A. J., Yao, X., Dix, J. A., Jin, B. J. & Verkman, A. S. Test of the 'glymphatic' hypothesis demonstrates diffusive and aquaporin-4-independent solute transport in rodent brain parenchyma. *Elife* **6**, 1–16 (2017).
13. Latham, T. W. Fluid motions in a peristaltic pump. (Massachusetts Institute of Technology (1966).
14. Jaffrin, M. Y. & Shapiro, A. H. Peristaltic Pumping. *Annu. Rev. Fluid Mech.* **3**, 13–37 (1971).
15. Shapiro, A. H., Jaffrin, M. Y., Weinberg, S. L. & Weinberg, L. Peristaltic pumping with long wavelengths at low Reynolds number. *J. Fluid Mech.* **37**, 799–825 (1969).
16. Abdelsalam, S. I. & Bhatti, M. M. The study of non-Newtonian nanofluid with hall and ion slip effects on peristaltically induced motion in a non-uniform channel. *RSC Adv.* **8**, 7904–7915 (2018).
17. Fung, Y. C. & Yih, C. S. Peristaltic transport. *J. Appl. Mech. Trans. ASME* **35**, 669–675 (1964).
18. Hartley, F T. Micromachined peristaltic pump. U.S. Patent No. 5,705,018 (1998).
19. Sorensen, G P., and T Akkas. Peristaltic pump and cassette. U.S. Patent No. 6,293,926 (2001).
20. Peclat, C. Peristaltic pump. U.S. Patent No. 6,102,678 (2000).
21. Shih, A. Y. *et al.* Two-photon microscopy as a tool to study blood flow and neurovascular coupling in the rodent brain. *J. Cereb. Blood Flow Metab.* **32**, 1277–1309 (2012).
22. Silverthorn, D. U., Ober, W. C., Garrison, C. W., Silverthorn, A. C. & Johnson, B. R. *Human physiology: an integrated approach*. (Pearson/Benjamin Cummings San Francisco, CA (2004).
23. Hall, J. E. *Guyton and Hall textbook of medical physiology e-Book*. (Elsevier Health Sciences (2015).
24. Martinac, A. D. & Bilston, L. E. Computational modelling of fluid and solute transport in the brain. *Biomech. Model. Mechanobiol.*, https://doi.org/10.1007/s10237-019-01253-y (2019).
25. Bilston, L. E., Fletcher, D. F., Brodbelt, A. R. & Stoodley, M. A. Arterial pulsation-driven cerebrospinal fluid flow in the perivascular space: a computational model. *Comput. Methods Biomech. Biomed. Eng.* **6**, 235–241 (2003).
26. Tithof, J., Kelley, D. H., Mestre, H., Nedergaard, M. & Thomas, J. H. Hydraulic resistance of periarterial spaces in the brain. *Fluids Barriers CNS* **16**, 1–13 (2019).
27. Herold, V. *et al. In vivo* measurement of local aortic pulse-wave velocity in mice with MR microscopy at 17.6 tesla. *Magn. Reson. Med. An Off. J. Int. Soc. Magn. Reson. Med.* **61**, 1293–1299 (2009).
28. Williams, R. *et al.* Noninvasive ultrasonic measurement of regional and local pulse-wave velocity in mice. *Ultrasound Med. Biol.* **33**, 1368–1375 (2007).
29. Winder, A. T., Echagarruga, C., Zhang, Q. & Drew, P. J. Weak correlations between hemodynamic signals and ongoing neural activity during the resting state. *Nat. Neurosci.* **20**, 1761–1769 (2017).
30. Mitchell, G. F., Jeron, A. & Koren, G. Measurement of heart rate and QT interval in the conscious mouse. *Am. J. Physiol. Circ. Physiol.* **274**, H747–H751 (1998).
31. Swoap, S. J. *et al.* Vagal tone dominates autonomic control of mouse heart rate at thermoneutrality. *Am. J. Physiol. Circ. Physiol.* **294**, H1581–H1588 (2008).
32. Chen, X., Gabitto, M., Peng, Y., Ryba, N. J. P. & Zuker, C. S. A gustotopic map of taste qualities in the mammalian brain. *Science (80-.).* **333**, 1262–1266 (2011).
33. Adams, M. D., Winder, A. T., Blinder, P. & Drew, P. J. The pial vasculature of the mouse develops according to a sensory-independent program. *Sci. Rep.* **8**, 1–12 (2018).
34. Goriely, A. *et al.* Mechanics of the brain: perspectives, challenges, and opportunities. *Biomech. Model. Mechanobiol.* **14**, 931–965 (2015).
35. Mihai, L. A., Chin, L. K., Janmey, P. A. & Goriely, A. A comparison of hyperelastic constitutive models applicable to brain and fat tissues. *J. R. Soc. Interface* **12** (2015).
36. Mihai, L. A., Budday, S., Holzapfel, G. A., Kuhl, E. & Goriely, A. A family of hyperelastic models for human brain tissue. *J. Mech. Phys. Solids* **106**, 60–79 (2017).
37. Budday, S. *et al.* Mechanical characterization of human brain tissue. *Acta Biomater.* **48**, 319–340 (2017).
38. Weickenmeier, J. *et al.* Brain stiffens post mortem. *J. Mech. Behav. Biomed. Mater.* **84**, 88–98 (2018).
39. Willinger, R., Taleb, L. & Pradoura, P. Head biomechanics: from the finite element model to the physical model. *in Proceedings of the International Research Council on the Biomechanics of Injury conference* **23**, 245–259 (1995).
40. Ruan, J. S., Khalil, T. B. & King, A. I. *Finite element modeling of direct head impact*. (1993).
41. Saboori, P. & Sadegh, A. Material modeling of the head's subarachnoid space. *Sci. Iran.* **18**, 1492–1499 (2011).
42. Galford, J. E. & McElhaney, J. H. A viscoelastic study of scalp, brain, and dura. *J. Biomech.* **3**, 211–221 (1970).
43. Oshio, K., Watanabe, H., Song, Y., Verkman, A. S. & Manley, G. T. Reduced cerebrospinal fluid production and intracranial pressure in mice lacking choroid plexus water channel Aquaporin-1. *FASEB J.* **19**, 76–78 (2005).
44. Yang, L. *et al.* Evaluating glymphatic pathway function utilizing clinically relevant intrathecal infusion of CSF tracer. *J. Transl. Med.* **11**, 1–9 (2013).
45. Louveau, A. *et al.* Structural and functional features of cns lymphatics. *Nature* **523**, 337–341 (2016).
46. Aspelund, A. *et al.* A dural lymphatic vascular system that drains brain interstitial fluid and macromolecules. *J. Exp. Med.* **212**, 991–999 (2015).
47. Norwood, J. N. *et al.* Anatomical basis and physiological role of cerebrospinal fluid transport through the murine cribriform plate. *Elife* **8**, 1–32 (2019).
48. Hladky, S. B. & Barrand, M. A. Mechanisms of fluid movement into, through and out of the brain: evaluation of the evidence. *Fluids Barriers CNS* **11**, 26 (2014).
49. Marmarou, A., Takagi, H. & Shulman, K. Biomechanics of brain edema and effects on local cerebral blood flow. *Adv. Neurol.* **28**, 345–358 (1980).
50. Mestre, H. *et al.* Aquaporin-4-dependent glymphatic solute transport in the rodent brain. *Elife* **7**, 1–31 (2018).
51. Huo, B.-X., Smith, J. B. & Drew, P. J. Neurovascular Coupling and Decoupling in the Cortex during Voluntary Locomotion. *J. Neurosci.* **34**, 10975–10981 (2014).
52. Umeda, Y. *et al.* Novel dynamic four-dimensional CT angiography revealing 2-type motions of cerebral arteries. *Stroke* **42**, 815–818 (2011).
53. Kuroda, J. *et al.* Cardiac cycle-related volume change in unrupured cerebral aneurysms: A detailed volume quantification study using 4-dimensional ct angiography. *Stroke* **43**, 61–66 (2012).
54. Herculano-Houzel, S. The human brain in numbers: a linearly scaled-up primate brain. *Front. Hum. Neurosci.* **3**, 31 (2009).
55. Asmar, R. *et al.* Assessment of arterial distensibility by automatic pulse wave velocity measurement: validation and clinical application studies. *Hypertension* **26**, 485–490 (1995).
56. Blacher, J., Asmar, R., Djane, S., London, G. M. & Safar, M. E. Aortic pulse wave velocity as a marker of cardiovascular risk in hypertensive patients. *Hypertension* **33**, 1111–1117 (1999).

57. Sarah GLADDISH & Chakravarthi RAJKUMAR. Repeatability of non-invasive measurement of intracerebral pulse wave velocity using transcranial Doppler. *Crit. Care Med.* **30**, 563–569 (2002).
58. Allen, J. & Murray, A. Age-related changes in peripheral pulse timing characteristics at the ears, fingers and toes. *J. Hum. Hypertens.* **16**, 711 (2002).
59. Keith Sharp, M., Carare, R. O. & Martin, B. A. Dispersion in porous media in oscillatory flow between flat plates: Applications to intrathecal, periarterial and paraarterial solute transport in the central nervous system. *Fluids Barriers CNS* **16**, 1–17 (2019).
60. Swartz, M. A. The physiology of the lymphatic system. *Adv. Drug Deliv. Rev.* **50**, 3–20 (2001).
61. Caggiati, A., Phillips, M., Lametschwandtner, A. & Allegra, C. Valves in Small Veins and Venules. *Eur. J. Vasc. Endovasc. Surg.* **32**, 447–452 (2006).
62. Weller, R. O. Pathology of cerebrospinal fluid and interstitial fluid of the CNS: significance for Alzheimer disease, prion disorders and multiple sclerosis. *J. Neuropathol. Exp. Neurol.* **57**, 885–894 (1998).
63. Davson, H. & Segal, M. B. *Physiology of the CSF and blood-brain barriers*. (CRC press (1996).
64. Ho, J. D. *et al.* Crystal structure of human aquaporin 4 at 1.8 A and its mechanism of conductance. *Proc. Natl. Acad. Sci. USA* **106**, 7437–7442 (2009).
65. Agre, P. *et al.* Aquaporin water channels - From atomic structure to clinical medicine. *J. Physiol.* **542**, 3–16 (2002).
66. Speake, T., Freeman, L. J. & Brown, P. D. Expression of aquaporin 1 and aquaporin 4 water channels in rat choroid plexus. *Biochim. Biophys. Acta - Biomembr.* **1609**, 80–86 (2003).
67. Brown, P. D., Davies, S. L., Speake, T. & Millar, I. D. Molecular mechanisms of cerebrospinal fluid production. *Neuroscience* **129**, 957–970 (2004).
68. Costanzo, F. & Miller, S. T. An arbitrary Lagrangian–Eulerian finite element formulation for a poroelasticity problem stemming from mixture theory. *Comput. Methods Appl. Mech. Eng.* **323**, 64–97 (2017).
69. Vinje, V. *et al.* Respiratory influence on cerebrospinal fluid flow – a computational study based on long-term intracranial pressure measurements. *Sci. Rep.* **9**, 1–13 (2019).
70. Holter, K. E. *et al.* Interstitial solute transport in 3D reconstructed neuropil occurs by diffusion rather than bulk flow. *Proc. Natl. Acad. Sci.* **2017**, 06942, https://doi.org/10.1073/pnas.1706942114 (2017).
71. Uldall, M., Botfield, H., Jansen-Olesen, I., Sinclair, A. & Jensen, R. Acetazolamide lowers intracranial pressure and modulates the cerebrospinal fluid secretion pathway in healthy rats. *Neurosci. Lett.* **645**, 33–39 (2017).
72. Formaggia, L., Quarteroni, A. & Veneziani, A. *Cardiovascular Mathematics: Modeling and simulation of the circulatory system*. **1**, (Springer Science & Business Media (2010).
73. Donea, J., Huerta, A., Ponthot, J. & Ferran, A. Chapter 14 Arbitrary Lagrangian-Eulerian Methods. *Encycl. Comput. …* 1–25 (2004).
74. Fernández, M. A., Formaggia, L., Gerbeau, J.-F. & Quarteroni, A. The derivation of the equations for fluids and structure. in *Cardiovascular Mathematics: Modeling and simulation of the circulatory system* (eds. Formaggia, L., Quarteroni, A. & Veneziani, A.) 77–121 (Springer Milan, https://doi.org/10.1007/978-88-470-1152-6_3 (2009).
75. Wick, T. Fluid-structure interactions using different mesh motion techniques. *Comput. Struct.* **89**, 1456–1467 (2011).
76. Sahni, O., Müller, J., Jansen, K. E., Shephard, M. S. & Taylor, C. A. Efficient anisotropic adaptive discretization of the cardiovascular system. *Comput. Methods Appl. Mech. Eng.* **195**, 5634–5655 (2006).
77. Leicht, T. & Hartmann, R. Error estimation and anisotropic mesh refinement for 3d laminar aerodynamic flow simulations. *J. Comput. Phys.* **229**, 7344–7360 (2010).
78. Formaggia, L., Micheletti, S. & Perotto, S. Anisotropic mesh adaptation in computational fluid dynamics: Application to the advection-diffusion-reaction and the Stokes problems. *Appl. Numer. Math.* **51**, 511–533 (2004).
79. Støverud, K. H., Langtangen, H. P., Haughton, V. & Mardal, K. A. CSF pressure and velocity in obstructions of the subarachnoid spaces. *Neuroradiol. J.* **26**, 218–226 (2013).
80. Yetkin, F. *et al.* Cerebrospinal fluid viscosity: a novel diagnostic measure for acute meningitis. *South Med J* **103**, 892–895 (2010).
81. Massi, F., Peng, J. W., Lee, J. P. & Straub, J. E. Simulation study of the structure and dynamics of the Alzheimer's amyloid peptide congener in solution. *Biophys. J.* **80**, 31–44 (2001).
82. Tseng, B. P. *et al.* Deposition of monomeric, not oligomeric, Aβ mediates growth of Alzheimer's disease amyloid plaques in human brain preparations. *Biochemistry* **38**, 10424–10431 (1999).

Acknowledgements

Author contributions

R.K. wrote the manuscript and prepared the figures. P.J.D. advised on all the biological aspects of the study. F.C. advised on all the computational aspects of the study. All authors reviewed the manuscript.

Competing interests

The authors declare no competing interests.

Additional information

Supplementary information is available for this paper at https://doi.org/10.1038/s41598-020-66887-w.

Correspondence and requests for materials should be addressed to F.C.

Reprints and permissions information is available at www.nature.com/reprints.

Publisher's note Springer Nature remains neutral with regard to jurisdictional claims in published maps and institutional affiliations.